Inorganic Chemistry
Article
pubs.acs.org/IC

Structural Flexibilities and Gas Adsorption Properties of One-Dimensional Copper(II) Polymers with Paddle-Wheel Units by Modification of Benzoate Ligands

Kiyonori Takahashi,[†] Norihisa Hoshino,[†,‡] Takashi Takeda,[†,‡] Shin-ichiro Noro,[§] Takayoshi Nakamura,[§] Sadamu Takeda,[⊥] and Tomoyuki Akutagawa*[,†,‡]

[†]Graduate School of Engineering, Tohoku University, Sendai 980-8579, Japan

[‡]Institute of Multidisciplinary Research for Advanced Materials (IMRAM), Tohoku University, 2-1-1 Katahira, Aoba-ku, Sendai 980-8577, Japan

[⊥]Graduate School of Science, Hokkaido University, Sapporo 060-0810, Japan

[§]Research Institute for Electronic Science, Hokkaido University, Sapporo 001-0020, Japan

Supporting Information

ABSTRACT: CO_2 and N_2 gas adsorption/desorption properties of one-dimensional copper(II) polymers with paddle-wheel units $[Cu^{II}_2(p\text{-XBA})_4(\text{pyrazine})]_\infty$ were successfully controlled through the tuning of interchain interactions by modification of para-substituent X groups on the benzoate (BA) ligands (X = Cl, Br, I, and OCH_3). Although none of the four crystals had sufficient void space to integrate the crystallization solvents, gate-opening gas adsorption and desorption behaviors coupled with structural phase transitions were observed for CO_2 (T = 195 K) and N_2 (T = 77 K), with differences depending on the precise substituent. van der Waals interchain interactions, specifically $\pi\cdots\pi$, halogen⋯π, and C−H⋯π contacts, were dominant in forming the crystal lattice; their magnitude was associated with gate-opening pressure and hysteresis behaviors. Both the type and magnitude of the interactions were evaluated by Hirshfeld surface analysis, which indicated that structural flexibility decreased as larger halogen atoms were included. Overall, weak interchain interaction and structural flexibility generated new void spaces to adsorb CO_2 and N_2 gases.

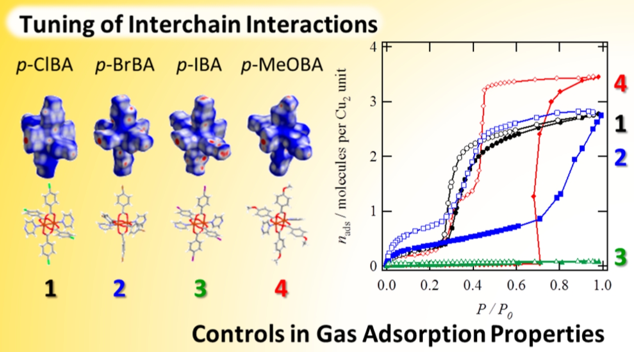

INTRODUCTION

One-dimensional (1D) metal coordination polymers are a particularly attractive research target given the potential to modulate their electrical conductivity,[1−3] magnetism,[4−6] and optical properties,[7−9] among other physical properties.[10] A great deal of research has tracked the correlation between the structural dimensionality and conduction properties of 1D MX and MMX systems (where M and X are metals and halogens, respectively);[11,12] most notable is the MMX-type $Pt_2(CH_3CS_2^-)_4I$ complex, which shows a high conductivity of 13 S cm^{-1}.[11] Furthermore, 1D quantum magnetic properties have been reported in single-chain magnets,[4,5,13] while gigantic third-order nonlinear-optical responses have been observed in mixed-valence NiX chains.[12] In these complexes, control of the interchain interactions plays an important role in forming the necessary 1D electronic structures. In addition, achieving these properties in bulk magnets requires the complete suppression of intermolecular magnetic interactions, necessitating precise control.[5]

Interesting gas adsorption/desorption properties in single crystals have been reported by Takamizawa et al. in the 1D complex $[M^{II}_2(BA)_4(pz)]_\infty$ (where M, BA, and pz are Cu and Rh, benzoate, and pyrazine, respectively).[14−18] Although these crystals have no void space in their structures, gate-opening CO_2, H_2, O_2, N_2, and Ar adsorption/desorption properties resulting from structural phase transition have been observed with the flipping motions of the BA ligands.

Among the various metal coordination complexes, excellent gas adsorption/desorption properties have been achieved in metal−organic frameworks (MOFs);[19] in this case, the relationship with structural flexibility has been extensively discussed with respect to host−guest and host−host intermolecular interactions.[19−21] Although the latter type provides the essential information to design new gas sorption molecular systems,[22] almost all MOF crystals have intrinsic void space filled by compatible crystallized solvent molecules; this makes evaluating host−host interactions difficult once the solvent has been removed, preventing sufficient examination. It is important to evaluate the relationship between the gas

Received: May 27, 2015
Published: September 18, 2015

DOI: 10.1021/acs.inorgchem.5b01168
Inorg. Chem. 2015, 54, 9423−9431

adsorption/desorption properties and host−host interactions of metal coordination polymer crystals that do not contain these intrinsic void spaces.

We have already reported control of the interchain interactions through the use of meta-substituted BA ligands (*m*-XBA) in $[Cu_2(m\text{-XBA})_4(pz)]_\infty$ crystals (X = F, Cl, and CH_3).[23] This species decreased the crystal symmetry and allowed the void space to be filled by CH_3CN. CO_2 was then adsorbed through a gate-opening mechanism once the solvent was removed. Alternatively, $[Cu^{II}_2(p\text{-IBA})_4(pz)]_\infty$, as reported by Burrows et al.,[24] showed higher crystal symmetry with the absence of crystallization solvents in the structure. We have taken advantage of this feature and herein report the syntheses, crystal structures, and CO_2 (T = 195 K) and N_2 (T = 77 K) gas adsorption/desorption properties of four 1D copper(II) polymer crystals containing paddle-wheel units: $[Cu^{II}_2(p\text{-ClBA})_4(pz)]_\infty$ (**1**), $[Cu^{II}_2(p\text{-BrBA})_4(pz)]_\infty$ (**2**), $[Cu^{II}_2(p\text{-IBA})_4(pz)]_\infty$ (**3**), and $[Cu^{II}_2(p\text{-MeOBA})_4(pz)]_\infty$ (**4**) (*p*-ClBA = *p*-chlorobenzoate, *p*-BrBA = *p*-bromobenzoate, *p*-IBA = *p*-iodobenzoate, and *p*-MeOBA = *p*-methoxybenzoate). Corresponding structures are provided in Chart 1. Changes in the interchain interactions as a result of modification of the ligands were tracked through monitoring the relationship between gas sorption and structural flexibility using Hirshfeld surface analysis.

Chart 1. Molecular Structures of the Four *p*-XBA Ligands and the pz Ligand Used in the Copper(II) Coordination Polymers 1−4

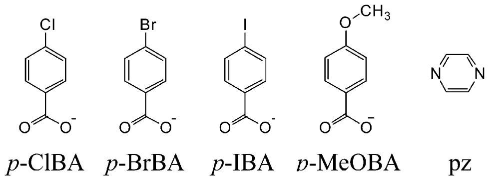

■ EXPERIMENTAL SECTION

Crystal Preparation. Commercially available chemical reagents were employed for crystal growth without further purification. Single crystals of **3** (yield 22%) were obtained according to a previously developed method.[24] Single crystals obtained from *p*-fluorobenzoate ligands were of significantly lower quality, making it difficult to evaluate the crystal structure and physical properties and precluding their inclusion here.

Crystals of **1** were prepared as follows: A mixture of $Cu(OAc)_2\cdot H_2O$ (4.2×10^{-4} mol) and *p*-chlorobenzoic acid (1.8×10^{-3} mol) in acetone (30 mL) and methanol (MeOH; 10 mL) was prepared and afforded the crystalline $[Cu_2(p\text{-ClBA})_4]$ dimer (91 mg) after several days. These were then dissolved in benzyl alcohol (5 mL), MeOH (5 mL), and acetone (2 mL), after which pz molecules were allowed to diffuse into the solution, resulting in tiny, green, needle-shaped single crystals of **1** (yield 36%).

Crystals of **2** were prepared as follows. First, $CuCl_2$ (3.8×10^{-4} mol) and *p*-bromobenzoic acid (1.0×10^{-3} mol) were dissolved in MeOH (5 mL) and diethyl ether (5 mL) in the presence of trimethylamine (50 mg). The blue $[Cu_2(p\text{-BrBA})_4]$ dimer rapidly precipitated out of solution and was collected and washed with MeOH. The obtained dimer (48 mg) was then dissolved in 2-(2-ethoxyethoxy)ethyl acetate (10 mL) and kept under pz vapor, resulting in tiny, green, needle-shaped single crystals of **2** (yield 15%). Crystals of **4** (yield 73%) were obtained by a method similar to that of **2**, this time using *p*-methoxybenzoic acid instead of *p*-bromobenzoic acid.

Elem anal. Calcd for **1** ($C_{32}H_{20}O_8N_2Cl_4Cu_2$): C, 46.34; H, 2.43; N, 3.38. Found: C, 46.63; H, 2.60; N, 3.45. Calcd for **2** ($C_{32}H_{20}O_8N_2Br_4Cu_2$): C, 38.16; H, 2.00; N, 2.78. Found: C, 38.32; H, 2.17; N, 2.89; H, 1.69; N, 2.34. Found: C, 32.18; H, 1.90; N, 2.41. Calcd for **4** ($C_{36}H_{32}O_{12}N_2Cu_2$): C, 53.27; H, 3.97; N, 3.45. Found: C, 53.00; H, 4.11; N, 3.53.

Single-Crystal X-ray Structural Analysis. High-quality single crystals of **1** suitable for single-crystal X-ray structural analysis were grown by mixing $Cu(OAc)_2\cdot H_2O$ (2.0×10^{-4} mol) and *p*-chlorobenzoic acid (4.16×10^{-4} mol) in hot MeOH (20 mL). The resulting blue solution was filtered to remove any solid particles and subjected to pz vapor, forming green single crystals of **1**. Single crystals of **4** were similarly obtained, this time by replacing *p*-chlorobenzoic

Table 1. Crystal Data, Data Collection, and Reduction Parameters

	1	**2**	**3**	**4**
chemical formula	$C_{16}H_{10}NO_4Cl_2Cu$	$C_{16}H_{10}NO_4Br_2Cu$	$C_{16}H_{10}NO_4I_2Cu$	$C_{36}H_{32}N_2O_{12}Cu_2$
fw	414.71	503.61	597.61	811.75
space group	$C2/m$ (No. 12)	$I\bar{4}$ (No.82)	$I4_1/a$ (No. 88)	$P\bar{1}$ (No. 2)
a, Å	16.4021(6)	18.4317(4)	18.7948(4)	10.1765(3)
b, Å	9.7641(3)			10.6471(3)
c, Å	12.2367(4)	19.5866(4)	19.6996(4)	16.9602(5)
α, deg				76.417(2)
β, deg	122.3890(17)			75.147(2)
γ, deg				77.005(2)
V, Å^3	1655.15(10)	6654.1(3)	6958.8(3)	1699.83(9)
Z	4	16	16	2
T, K	110	112	100	110
D_{calc}, g cm^{-3}	1.664	2.011	2.282	1.586
μ, cm^{-1}	5.023	7.676	298.160	21.416
reflns measured	5894	38255	29446	18054
indep reflns	1590	6102	3179	5998
reflns used	1590	6102	3179	5998
R_{int}	0.0779	0.0530	0.0844	0.0814
R_1[a]	0.1038	0.0990	0.0683	0.0973
$R_w(F_2)$[a]	0.3324	0.2762	0.1756	0.1506
GOF	1.137	1.053	1.188	1.123

[a] $R_1 = \sum||F_o| - |F_c||/\sum|F_o|$ and $R_w = (\sum w(|F_o| - |F_c|)2/\sum wF_o^2)^{1/2}$.

acid with *p*-methoxybenzoic acid. The single crystals of **3** used for this analysis were the same ones developed in the previously mentioned procedure, while single crystals of **2** were grown in a similar manner, although by using *p*-bromobenzoic acid instead of *p*-iodobenzoic acid (Figures S2–S4).[24]

Each single crystal was mounted on thin polyimide films (MiTeGen MicroMounts) using oil (Hampton Research Parabar 10312). Temperature-dependent crystallographic data (Table 1) were collected using a Rigaku RAPID-II diffractometer equipped with a rotating anode fitted with a multilayer confocal optic using Cu Kα (λ = 1.54187 Å) radiation. Calculations were performed using Crystal Structure software packages.[25−27] Parameters were refined using anisotropic temperature factors except for hydrogen atoms; these were refined using the riding model. The void space was calculated using the *SQUEEZE* tool in *PLATON*.[28]

Hirshfeld Surface Analysis. Two-dimensional (2D) fingerprint plots were obtained through Hirshfeld surface analysis using *Crystal Explorer 3.1*.[29] Because the asymmetric structural units in crystal **4** were constructed from two unique pz molecules, the Hirshfeld surface calculations of crystals **1**–**4** were performed for the [Cu_2(*p*-XBA)$_4$(pz)$_2$] unit. Because the 4-fold rotation axis of crystal **2** resulted in the four crystallographically independent *p*-BrBA ligands of **2A**, **2B**, **2C**, and **2D**, four different Hirshfeld surfaces were analyzed. Likewise, two crystallographically independent *p*-IBA ligands of **3A** and **3B** were observed in crystal **3**, with *p*-IBA (**3B**) showing an orientational disorder of **3B** and **3B′**. This resulted in three distinct *p*-IBA environments, each of which was evaluated.[30]

Adsorption/Desorption Measurements. The N_2 and CO_2 adsorption/desorption isotherms were measured with the automatic volumetric adsorption apparatus BELSORP-max (BEL Japan) at 77 and 195 K, respectively. Before the measurements, the crystals were maintained at 380 K under a pressure of less than 10^{-2} Pa for 18 h in order to remove adsorbed molecules on the surface.

■ RESULTS AND DISCUSSION

Overview of Crystal Structures. Figure 1 shows the unit cell of crystal **1** viewed along the *b* axis, demonstrating that the 1D polymer chains were elongated along the *b* axis and the crystallization solvents were not observed in the crystal lattice. The same packing structures were observed in crystals **2**–**4** (Figure S10), suggesting that the introduction of para substituents resulted in efficient polymer packing through van der Waals interactions. The void spaces in crystals **3** and **4** were not predicted in *PLATON* calculations, although small void spaces of 44.1 and 22.5 Å^3 per [Cu_2(*p*-XBA)$_4$] unit were expected in crystals **1** and **2**, respectively. These spaces are insufficient to include crystallization solvents. Additionally, residual electron densities in differential Fourier analysis were consistent with structures lacking any kind of crystallization solvent. Finally, the vibrational spectra, elemental analyses, and thermogravimetry (TG) charts reinforce these observations (Figures S1 and S5).

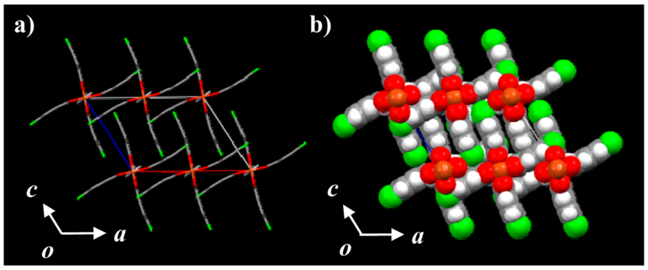

Figure 1. Packing structures of crystal **1** viewed along the *b* axis using the (a) stick and (b) CPK models.

Gas Adsorption/Desorption Isotherms. Figure 2a summarizes the CO_2 adsorption/desorption isotherms of crystals **1**–**4** at 195 K. The number of adsorption/desorption molecules (n_{ads}) per [Cu^{II}_2(*p*-XBA)$_4$(pz)] unit was plotted against the relative pressure P/P_0 from 10^{-5} to 1.0 for adsorption and from 1.0 to 10^{-2} for desorption. The CO_2 adsorption of crystals **1** and **2** was observed at relatively low CO_2 pressure of P/P_0 = 0.3 at n_{ads} = 0.5 mol mol^{-1} and P/P_0 = 0.7 at n_{ads} = 1.0 mol mol^{-1}, respectively. Further increasing P/P_0 for crystals **1** and **2** significantly increased n_{ads} at P/P_0 = 0.3 and 0.7, respectively; overall adsorption behaviors were different given the different X groups of Cl and Br. Finally, crystals **1** and **2** could adsorb approximately n_{ads} = 3.0 mol mol^{-1} of CO_2 at P/P_0 = 1.0, which was consistent with the formation of a new void space of about 180 Å^3 per [Cu^{II}_2(*p*-XBA)$_4$(pz)] unit between the polymers.[31]

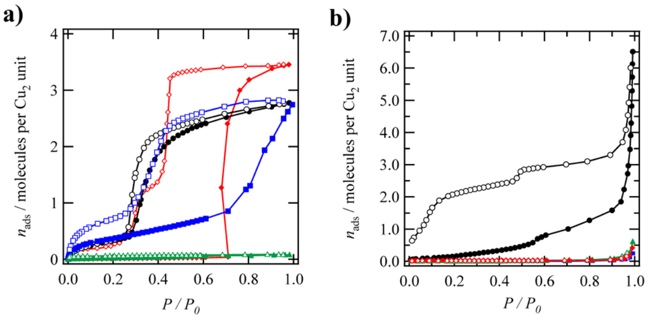

Figure 2. Gas adsorption/desorption isotherms of crystals **1** (black circle), **2** (blue square), **3** (green triangle), and **4** (red rhombus) for (a) CO_2 at 195 K and (b) N_2 at 77 K. The adsorption and desorption processes are represented by filled and empty symbols, respectively.

The hysteresis behaviors of crystals **1** and **2** for CO_2 adsorption/desorption processes were consistent with the gate-opening mechanism coupled with the structural phase transition.[31,32] The intrinsic small void spaces were insufficiently large to adsorb three CO_2 molecules, meaning that the added structural flexibility and resulting gate-opening mechanism accounts for the increased CO_2 adsorption space at relatively low gas pressures. However, although the lattice parameter and packing structure of crystal **3** were similar to those of crystal **2**, it did not exhibit CO_2 adsorption/desorption behavior. Meanwhile, crystal **4** did not exhibit adsorption at P/P_0 < 0.7, although sudden activity was observed beyond this point, accounting for a total of n_{ads} = 3.5 mol mol^{-1} through the formation of the new void space between polymer chains at P/P_0 = 1.0. The absence of intrinsic void space in crystal **4** was consistent with the lack of sorption behavior at lower pressures. Overall, these differences in the sorption activity were associated with differences in the interchain interactions and structural flexibility. The *p*-MeOBA ligand resulted in distinct activity due to the different kinds of van der Waals interactions that it elicits.

These results were consistent with differential scanning calorimetry (DSC) measurements (Figure S6). Upon cooling the samples to 180 K, the exothermic peaks in crystals **1** and **4** correspond to the CO_2 adsorption process coupled with the structural phase transition. However, thermal anomalies were not observed for crystal **3**, which was again consistent with the CO_2 adsorption isotherm. Although the CO_2 sorption of crystal **2** was confirmed in the CO_2 adsorption/desorption isotherm, there was no endothermic peak in the DSC measurements. The

CO_2 sorption equilibrium for the gate-opening mechanism was out of the measuring temperature range, which was consistent with a relatively higher P/P_0 value of crystal **2** than the other crystals.

Figure 2b shows the N_2 adsorption/desorption isotherms of crystals **1**−**4** at 77 K. Only crystal **1** showed any activity that was consistent with the hysteresis behavior of the gate-opening mechanism. A gradual increase in n_{ads} was observed at $P/P_0 < 0.5$ during adsorption, an effect that accelerated somewhat at $P/P_0 > 0.55$. The rapid increase around $P/P_0 = 1.0$ was due to liquefaction of N_2 gas, where about 3.0 mol of N_2 gas per $[Cu^{II}_2(p\text{-ClBA})_4(pz)]$ unit was adsorbed into the interchain space. Assuming a molecule volume of about 60 Å^3,[33] this means that a new void space of approximately 180 Å^3 per $[Cu^{II}_2(p\text{-ClBA})_4(pz)]$ unit was generated. This quantity of N_2 was effectively retained in the desorption process until about $P/P_0 = 0.5$, with discontinuous loss below that point.

1D Coordination Polymer Chains. Figure 3 shows the molecular structures of crystals **1**−**4**. Four *p*-XBA ligands were coordinated to two copper(II) ions to form the paddle-wheel type copper(II) binuclear coordination structure, while each paddle-wheel unit was linearly connected by axial pz ligands to form the 1D copper(II) polymer chains in crystals **1**−**4** along the *b*, *c*, *c*, and −*a* − *b* + *c* axes, respectively.

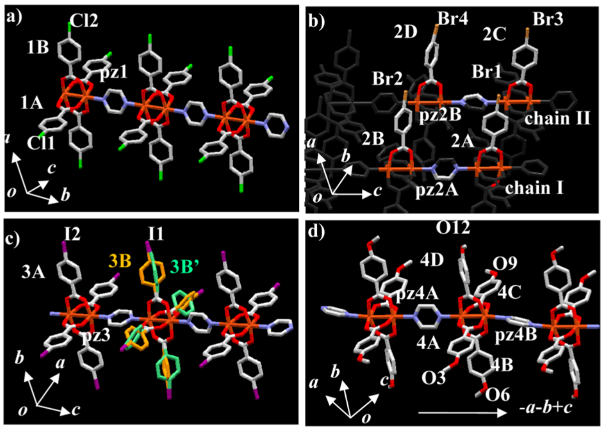

Figure 3. Molecular structures of the 1D copper(II) polymer chains and selected atomic numbering schemes for (a) **1**, (b) **2**, (c) **3**, and (d) **4**. Hydrogen atoms were omitted for clarify.

The symmetrical space group of $C2/m$ for crystal **1** afforded two kinds of crystallographically independent *p*-ClBA ligands, **1A** and **1B**, including Cl1 and Cl2 substituents, respectively, and one pz ligand (Figure 3a). Crystal **2** exhibited higher symmetry, and the space group was $I\bar{4}$, where two distinct polymer chains, I and II, formed crystallographically independent structural units. Among them, two kinds of crystallographically independent *p*-BrBA ligands, **2A** and **2B**, including Br1 and Br2 substituents, respectively, were observed in chain I, whereas **2C** and **2D**, including Br3 and Br4 substituents, respectively, were observed in chain II (Figure 3b). Furthermore, two crystallographically independent pz ligands, **pz2A** and **pz2B**, were coordinated to the paddle-wheel units at axial positions in chains I and II, respectively.

The symmetry of crystal **3** ($I4_1/a$) was even higher, with two kinds of crystallographically independent *p*-IBA ligands, **3A** and **3B**/**3B′**; **3B** and **3B′** describe the orientational disorder, with occupancy factors of 0.3 and 0.7, respectively. The dihedral angle between the aromatic C_6H_4 rings of the disordered **3B** and **3B′** ligands (orange and yellow-green rings in Figure 3c, respectively) was 72.5°. Finally, the lower crystal symmetry of crystal **4**, represented by the $P\bar{1}$ space group, results from the low symmetry of the *p*-MeOBA ligands. One $[Cu^{II}_2(p\text{-MeOBA})_4(pz)_2]$ paddle-wheel unit served as a crystallographically independent structural unit, while four kinds of *p*-MeOBAs ligands, **4A**, **4B**, **4C**, and **4D**, were coordinated to the Cu1 and Cu2 sites. In addition, two pz ligands, **pz4A** and **pz4B**, were axially coordinated to Cu1 and Cu2, respectively.

Intermolecular Interactions. Figure 4 shows the interchain interactions in crystals **1**−**4**, while Table 2 summarizes their type, distance, and angle. The π···π interaction is among the most dominant ones in crystal **1**. One such interaction was observed, with pairs of **1B**···**pz1** with average π···π distances of 3.39 Å. Another parallel arrangement between π···π planes was observed with pairs of **1A**···**1A**, but this was not regarded as a π···π interaction because of the unusually long distance (3.88 Å) for this interaction. Another weak van der Waals interaction of Cl1···C8, with a distance of 3.27 Å, was assumed to be an induced-dipole interaction and so was not assigned as a halogen···π interaction given the lack of aromatic character of the C8 atom of the carboxylate moiety.

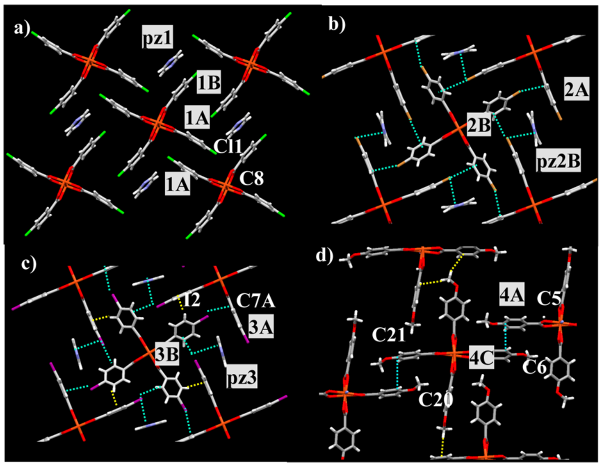

Figure 4. Interchain interactions around *p*-XBA ligands in crystals **1**−**4**: (a) π···π stacking interaction of **1B**···**pz1** in crystal **1**; (b) Br···π interactions (green lines) in crystal **2**; (c) I···π (green lines) and C−H···π (yellow lines) interactions in crystal **3**; (d) C−H···π interactions between hydrogen atoms of the CH_3O- group in the *p*-MeOBA ligands and the nearest-neighboring *p*-MeOBA ligands in crystal **4** (yellow line).

The 1D copper(II) polymer chains in crystal **2** were elongated along the *c* axis and formed a part of the 2D system resulting from interchain Br···π interactions within the *ab* plane (Figure 4b). The dihedral angle between the two aromatic C_6H_4Br rings of the nearest-neighboring *p*-BrBA ligands (ϕ_1; Chart 2) was 33.1−52.3°, while the π plane of the **pz2** ring interacted with the Br group of *p*-BrBA in the absence of an effective π···π interaction (Figure 5a). Meanwhile, the *p*-BrBA ligands **2A** and **2B** in chain I interacted with the **pz2B** ligand in chain II, whereas **2C** and **2D** in chain II interacted with **pz2A** in chain I (Figure 4b). In addition, C−H···π interactions were observed between the **2D** ligand and the π plane of the **2C** one (Figure 5b). Each of the four crystallographically independent *p*-BrBA ligands in crystal **2** exhibited different types of interchain interactions, including Br···π and C−H···π.

Table 2. Type, Distance, and Dihedral Angles of Interchain Interactions in Crystals 1−4

crystal	ligand	C−H···π[a]	X···π[b]	π···π[c]	p_1,[d] Å	ϕ_1,[e] deg	ϕ_2,[f] deg	d_{X-C},[g] Å	$d_{CH-\pi}$,[h] Å
1	**1A**	-	-	-	3.88	0	-	-	-
	1B	-	-	○	3.39	-	3.39	3.27	-
2	**2A**	-	○	-	-	33.1	9.14	3.47	-
	2B	-	○	-	-	33.1	-	3.32	-
	2C	○	○	-	-	52.3	8.13	3.30	2.575
	2D	○	○	-	-	52.3	-	3.36	*Acceptor*
3	**3A**	○	○	-	-	60.2	7.99	3.30	*Acceptor*
	3B	○	○	-	-	60.2	-	3.45	2.411
	3B′	○	○	-	-	48.5	-	3.45	2.739
4	**4A**	○	-	-	3.88	0	-	-	2.864
	4B	○	-	-	-	62.5	-	-	2.801
	4C	○	-	○	3.43	0	-	-	2.827
	4D	○	-		-	62.5	-	-	2.611

[a] The existence of effective C−H···π interactions. "○" and "−" are the presence and absence of corresponding interchain interactions. [b] The existence of effective halogen···π interactions. [c] The existence of π···π interactions in π···π stacking planes, where the dihedral angles (ϕ_1) and distances between neighboring π···π planes were evaluated. [d] p_1 was the nearest C···C distance between two neighboring *p*-XBA···*p*-XBA and/or *p*-XBA···pz ligands. [e] ϕ_1 was the interplanar angle of two neighboring *p*-XBA ligands. [f] ϕ_2 was the interplanar angle of two neighboring *p*-XBA and pz ligands. [g] d_{X-C} was the X(halogen)···C distance for the nearest-neighboring atoms in X(halogen)···π interactions. [h] $d_{CH-\pi}$ was the C−H···C(π plane) distance for the nearest-neighboring atoms in C−H···π interactions. *Acceptor* corresponds to the accepting character in the C−H···π interaction at the π plane.

Chart 2. Schematic View of p_1, ϕ_1, ϕ_2, and d_{X-C} Structural Parameters

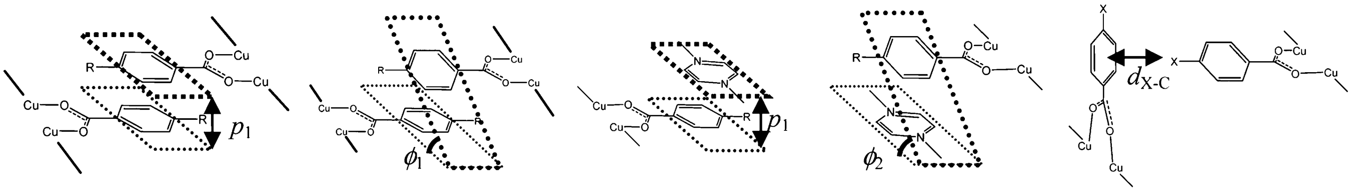

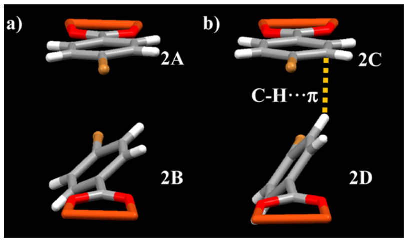

Figure 5. Two potential types of *p*-BrBA···*p*-BrBA interactions between neighboring *p*-BrBA ligands in crystal **2**: (a) **2A**···**2B**; (b) **2C**···**2D**.

Intermolecular interactions between iodine atoms and the π plane in *p*-IBA ligands were observed in crystal **3** (Figure 4c). Notably, the magnitude of the I···π interaction in crystal **3** was greater than that of the Br···π interaction in crystal **2**. Likewise, the packing structure of **3** was denser than that of **2** based on D_{calc} (Table 1) and void space calculation. The C−H···π interaction also apparently played an important role in determining the packing structure because the C···H distances between carbon atoms in the π plane of the **3A** ligand and the hydrogen atom of the **3B**/**3B′** plane were shorter than the sum of the van der Waals atomic radii. Crystal **4** showed different interaction modes, where partial π-plane overlap between **4C** ligands revealed π···π interaction with a stacking structural parameter of $d_{C20-C21}$ = 3.43 Å and ϕ_1 = 0°.

The effective C−H···π interactions between the hydrogen atoms of the CH_3O− group and the π plane of the *p*-MeOBA and/or pz ligands were confirmed by analyzing the 2D network (Figure 4d), with C−H···O interactions observed at the hydrogen and oxygen atoms of the CH_3O− and/or $-COO^-$ groups. Because the types of interchain interactions at the four independent *p*-MeOBA ligands were different from each other, the magnitudes exhibited an anisotropic character. The sizes of the halogen atoms in crystals **1**−**3** were also different from each other, leading to changes in the magnitudes of the interactions. Because the interchain interaction in crystal **4** was completely different from the others, the anisotropic structural flexibility directly impacted the CO_2 gas adsorption/desorption properties in a different manner.

The energies of π···π and C−H···π interactions have previously been found to be in the ranges 8.4−42 and 2.1−8.4 kJ mol^{-1}, respectively.[34] Although there was insufficient information about the magnitude of the halogen···π interactions, the complex formation energy between benzene (and/or toluene) and bromine (and/or iodine) in halogen···π interactions was estimated by Monte Carlo,[35] density functional theory, and Moeller−Plesset second-order perturbation theory calculations using the crystal structures of halogenated trityl alcohol.[36,37] The energy of halogen···π interactions was approximately 5.93−21.7 kJ mol^{-1}, with I···π interactions stronger than Br···π ones. This energy difference has been discussed theoretically.[38] The diameter of the σ hole corresponds to electrostatically positive potential region, for the iodine atom is larger than that of bromine, which accounted for the stronger interaction and played a significant role in forming effective and rigid interchain interactions. The structural flexibility decreased from **1** to **2** to **3**, which is in line with the observed gas adsorption/desorption properties.

Hirshfeld Surface Analysis. Hirshfeld surface analysis was applied to evaluate the structural flexibility and magnitude of each interchain interaction in crystals **1**−**4**. d_{norm} in the Hirshfeld surface map is defined in eq 1[30]

$$d_{\text{norm}} = [(d_{\text{i}} - r_{\text{i}}^{\text{vdW}})/r_{\text{i}}^{\text{vdW}}] + [(d_{\text{e}} - r_{\text{e}}^{\text{vdW}})/r_{\text{e}}^{\text{vdW}}] \qquad (1)$$

where d_{i}, d_{e}, $r_{\text{i}}^{\text{vdW}}$, and $r_{\text{e}}^{\text{vdW}}$ are the distance from the surface to the nearest-neighboring atom interior, the distance from the surface to the nearest-neighboring atom exterior, the van der Waals radii of the nearest-neighboring atom interior to the surface, and the van der Waals radii of the nearest-neighboring atom exterior to the surface, respectively. This analysis is useful for evaluating the closest intermolecular atomic contacts, even in complex crystal structures.[30] In such an analysis, the color scheme corresponds to the magnitude of intermolecular interactions, ranging from strong (red) to middle (white) to weak (blue). For example, this means that short intermolecular contacts of less than the sum of the van der Waals radii are represented in red.

When the crystal structures are similar to each other, the differences in the intermolecular interactions can be discussed on the basis of color. Figure 6 provides the d_{norm} surfaces for crystals **1**−**4**. Overall, the percentage of red area around halogen substituents increased from crystal **1** to **2** and **3**. Meanwhile, the red sections of the d_{norm} surface in crystal **4** were observed around aromatic rings and CH_3O− groups as a result of C−H⋯π interactions. Hirshfeld surface analysis enables us to evaluate the nearest-neighboring atomic contacts for each intermolecular interaction based on the 2D fingerprint plots, which included several types of intermolecular interactions.

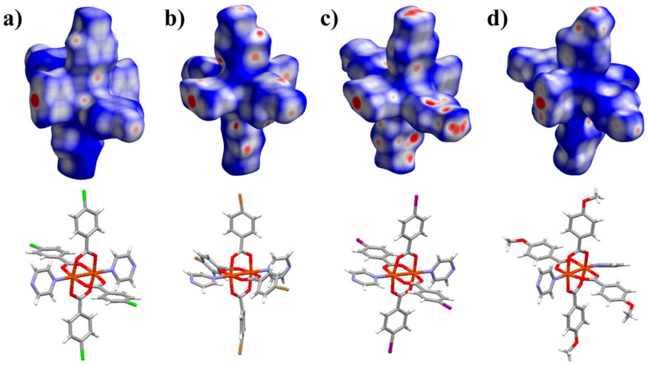

Figure 6. Visualization of intermolecular interactions using Hirshfeld surface analysis, with Hirshfeld surfaces (upper figures) and molecular structures (lower figures) for (a) **1**, (b) **2**, (c) **3**, and (d) **4**. The surface is defined using the parameter d_{norm} and was rescaled from −0.3 (red) to 0.8 (blue).

From the 2D fingerprint plots, the percentages of each kind of interatomic interaction present in the species can be represented in the form of a histogram. When the histograms of different crystals were similar to each other, the intermolecular interactions for these crystals resemble each other. Figure 7 provides histograms summarizing the types of atomic contacts in each crystal. Because the histograms from each paddle-wheel unit were similar (Figure S13), the average percentage was represented in crystals **2** and **3**. Although the percentage of van der Waals type H⋯H interactions between nearest-neighboring hydrogen atoms accounts for a significant portion of the overall interactions, the stabilization they provide is quite small in magnitude because these interactions are between the same species.[39] Halogen⋯π, π⋯π, and C−H⋯π interactions contributed much more substantially, with the percentage of interatomic interactions including halogen species at about 35%. The distribution of the types of intermolecular interactions in crystal **4** was notably different from those in crystals **1**−**3**.

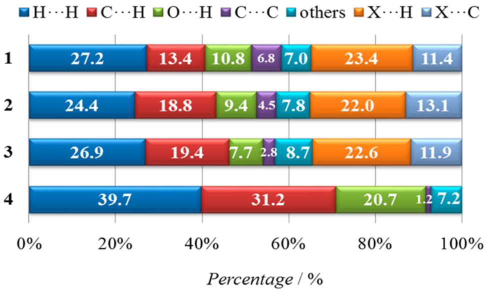

Figure 7. Histograms summarizing the types of atomic contacts between the nearest-neighboring species, based on 2D fingerprint plots. The average percentages in crystals **2** and **3** were utilized because of the existence of multiple crystallographically independent coordination polymer chains.

In general, the strength of noncovalent dispersion-type intermolecular interactions was proportional to d^{-6}, where d is the distance between the two atoms. Upon analysis of the 2D fingerprint plot, it is therefore important to discuss the $d_{\text{i}} + d_{\text{e}}$ distance less than the sum of the van der Waals radii of the two atoms that are closest to each other. When this value is short, the intermolecular interactions should be strong. Figure 8 summarizes the 2D fingerprint plots for C⋯H interatomic contacts in crystals **1**−**4**. The red line corresponds to a $d_{\text{i}} + d_{\text{e}}$ distance that is equivalent to the sum of the van der Waals radii of carbon (1.70 Å) and hydrogen (1.20 Å), while the red area therefore corresponds to the section that would contain effective C⋯H contacts. Gray sections indicate all non-C⋯H interactions, while blue sections indicate C⋯H contacts; the percentage of interactions that fall in the latter category is summarized at the bottom of each plot. Because the blue areas for crystals **2** and **3** extended into the red area (Figure 8b,c), many of the C⋯H contacts effected positive interatomic interaction. On the contrary, there were no effective interatomic C⋯H contacts in crystal **1**. Two of the four independent $[Cu_4(p\text{-BrBA})_4(pz)_2]$ units in crystal **2** had effective C−H⋯π contacts between the hydrogen atom of the **2C** ligand and the π plane of the **2D** one (Figure 5b), whereas C−H⋯π interactions were not observed for **2A** and **2B** (Figure 5a). Different interatomic interactions were also observed in the 2D fingerprint plots for other chains in crystal **2** (Figure S16). Overall, C⋯H intermolecular interactions were stronger in crystal **3** than in crystal **2**, while both the type and magnitude of interchain interactions in crystal **4** were different.

Figures 9 and 10 summarize the 2D fingerprint plots for halogen⋯C and halogen⋯H interatomic contacts in crystals **1**−**3**. Although the amount of the blue area that extends into the red area is similar between **1** and **2**, the overall effects are not comparable. Although the effective interatomic interaction between the chlorine atom and the carbon atom of the carboxylate unit was observed in crystal **1**, there was an induced dipole Cl⋯C one. The intermolecular interactions related to the chlorine atom in crystal **1** resulted in weaker effects than those related to the bromine atom in crystal **2** because of the absence of the character of the halogen⋯π interaction between the chlorine and carbon atoms. Meanwhile, crystal **3** shows far more blue area located within the red region (Figures 9c and

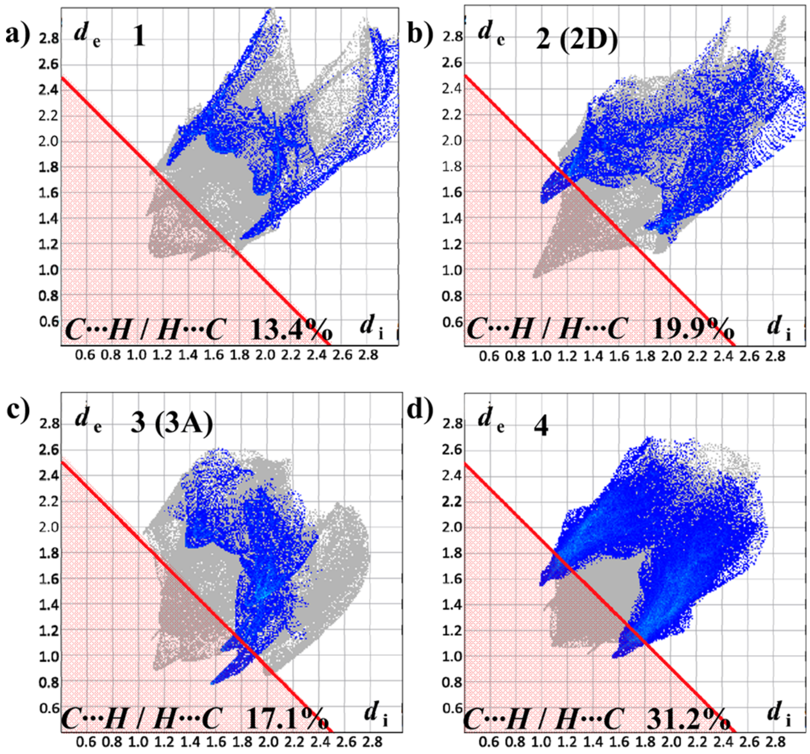

Figure 8. 2D fingerprint plots of C···H contacts (blue area) along with the other kinds (gray area) for (a) **1**, (b) **2**, (c) **3**, and (d) **4**. Red areas correspond to interatomic contacts of less than the sum of the van der Waals radii for the carbon and hydrogen atoms.

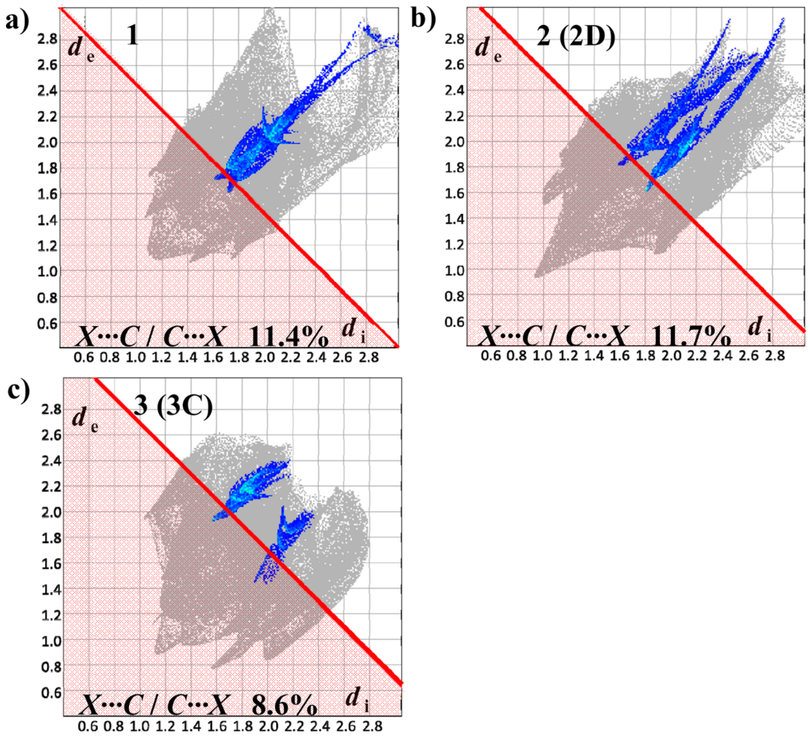

Figure 9. 2D fingerprint plots of halogen···C contacts (blue area) in addition to all other kinds of interatomic contacts (gray area) for (a) **1**, (b) **2**, and (c) **3**. Red areas correspond to interatomic contacts of less than the sum of the van der Waals radii for the halogen and carbon atoms.

10c), suggesting that the iodine atom provides stronger interaction overall.

Hirshfeld surface analysis demonstrates the magnitude and type of intermolecular interactions and structural flexibilities for similar molecular structures in a qualitative manner. Results indicate that crystal **3** showed the least structural flexibility, followed by crystal **2** and finally crystal **1**. However, crystal **4** showed a completely different structure because the primary effective interatomic interaction was C−H···*π*. Overall, the Hirshfeld surface of crystal **4** indicated much greater flexibility

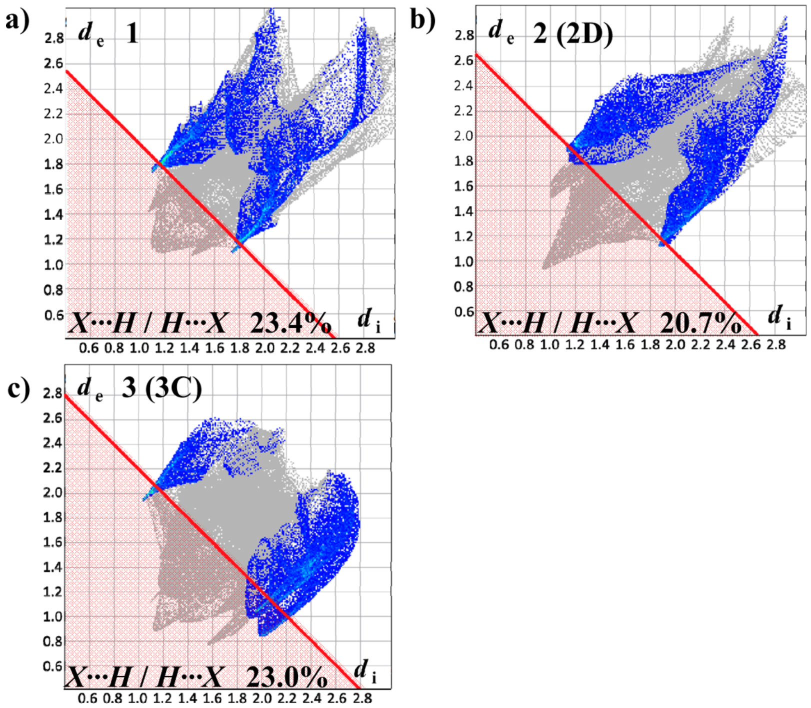

Figure 10. 2D fingerprint plots of halogen···H contacts (blue area) in addition to all other kinds of interatomic contacts (gray area) for (a) **1**, (b) **2**, and (c) **3**. Red areas correspond to interatomic contacts of less than the sum of the van der Waals radii for the halogen and hydrogen atoms.

than that of crystal **3**. The gate-opening pressure and hysteresis behavior of crystal **4** were also different from those in crystals **1** and **2**. Apparently, the introduction of the bulky and flexible CH_3O group into crystal **4** resulted in anisotropic interchain interactions and unusual gate-opening CO_2 adsorption/desorption properties. However, because N_2 adsorption was not observed in crystal **4**, its crystal structure was likely more rigid than that of crystal **1**.

Flexible MOFs exhibited the gate-opening CO_2 adsorption/desorption behavior in the absence of N_2 behavior, the difference of which was associated with the polarizability and quadrupole moment of the CO_2 molecule. The high magnitude of polarizability and quadrupole moment of the CO_2 molecule can interact and open the crystal lattice for its adsorption.[40,41] On the contrary, N_2 adsorption/desorption behavior was observed on the crystal surface area in the absence of the formation of void space[41] and/or in the interchain space formed by the gate-opening mechanism.[31] Because the interchain interactions in crystal **1** were weaker than those of the other crystals, both the N_2 and CO_2 adsorption/desorption behaviors were only observed in crystal **1**. Much stronger interchain interactions in crystals **2** and **4** than those of crystal **1** showed only the CO_2 adsorption/desorption behavior in the absence of N_2 sorption behavior.

■ CONCLUSIONS

CO_2 and N_2 gas adsorption/desorption isotherms, single-crystal X-ray crystal structure analyses, and Hirshfeld surface analyses of 1D copper(II) polymers with paddle-wheel units bearing bulky substituents on the *p*-XBA ligands were examined for X = Cl, Br, I, and CH_3O. Although effective void space was not found in all crystal structures, the CO_2 gas adsorption/desorption isotherms at 195 K of crystals **1**, **2**, and **4** showed gate-opening sorption coupled with structural phase transition. Although crystal **3** had a similar lattice parameter and packing structure compared to crystal **2**, crystal **3** did not show CO_2 adsorption. Meanwhile, the gate-opening N_2 gas adsorption/desorption properties in crystal **1** were dominated by $\pi\cdots\pi$ interactions, even while $Br\cdots\pi$ and $I\cdots\pi$ interchain interactions played an important role in stabilizing the packing structures of crystals **2** and **3**, respectively. At the same time, weak $\pi\cdots\pi$ and $C-H\cdots\pi$ interactions were anisotropically observed in crystal **4**. The generated 2D fingerprint plots based on Hirshfeld surface analyses were consistent with the structural flexibility and gas adsorption properties. Overall, this suggests that favored adsorption gases and the gate-opening pressure can be modified by altering interchain interactions through chemical modifications of the ligand structure. Intermolecular host−host interactions were directly associated with gas adsorption/desorption properties, enabling us to design new gas adsorption materials by tuning the bulkiness of the ligand structure through chemical modification.

■ ASSOCIATED CONTENT

Ⓢ Supporting Information

The Supporting Information is available free of charge on the ACS Publications website at DOI: 10.1021/acs.inorgchem.5b01168.

TG diagrams, atomic numbering scheme, structural analyses of **1**−**4**, IR spectra in KBr pellets, Hirshfeld surface analyses, and DSC measurements in a CO_2 atmosphere (PDF)

X-ray crystallographic data in CIF format (CIF)

■ AUTHOR INFORMATION

Corresponding Author

*E-mail: akuta@tagen.tohoku.ac.jp.

Notes

The authors declare no competing financial interest.

■ ACKNOWLEDGMENTS

This work was supported by a Grant-in-Aid for Science Research from the Ministry of Education, Culture, Sports, Science, and Technology of Japan and by Management Expenses Grants for National Universities of Japan and Grant-in-Aid for JSPS Fellows 25-9150.

■ REFERENCES

(1) Lin, P.; Henderson, R. A.; Harrington, R. W.; Clegg, W.; Wu, C.-D; Wu, X.-T. *Inorg. Chem.* **2004**, *43*, 181−188.

(2) Liu, S. Q.; Kuroda-Sowa, T.; Konaka, H.; Suenaga, Y.; Maekawa, M.; Mizutani, T.; Ning, G. L.; Munakata, M. *Inorg. Chem.* **2005**, *44*, 1031−1036.

(3) Delgado, S.; Sanz Miguel, P. J.; Priego, J. L.; Jimenez-Aparicio, R.; Gomez-Garcia, C. J.; Zamora, F. *Inorg. Chem.* **2008**, *47*, 9128−9130.

(4) Miyasaka, H.; Julve, M.; Yamashita, M.; Clérac, R. *Inorg. Chem.* **2009**, *48*, 3420−3437.

(5) Coulon, C.; Miyasaka, H.; Clérac, R. *Struct. Bonding (Berlin)* **2006**, *122*, 163−206.

(6) Noro, S.; Miyasaka, H.; Kitagawa, S.; Wada, T.; Okubo, T.; Yamashita, M.; Mitani, T. *Inorg. Chem.* **2005**, *44*, 133−146.

(7) Sui, B.; Zhao, W.; Ma, G.; Okamura, T.; Fan, J.; Li, Y.-Z.; Tang, S.-H.; Sun, W.-Y.; Ueyama, N. *J. Mater. Chem.* **2004**, *14*, 1631−1639.

(8) Li, L. K.; Song, Y. L.; Hou, H. W.; Fan, Y. T.; Zhu, Y. *Eur. J. Inorg. Chem.* **2005**, *2005*, 3238−3249.

(9) Iwasa, Y.; Funatsu, E.; Hasegawa, T.; Koda, T.; Yamashita, M. *Appl. Phys. Lett.* **1991**, *59*, 2219−2221.

(10) Yamada, T.; Sadakiyo, M.; Kitagawa, H. *J. Am. Chem. Soc.* **2009**, *131*, 3144−3145.

(11) Kitagawa, H.; Onodera, N.; Sonoyama, T.; Yamamoto, M.; Fukawa, T.; Mitani, T.; Seto, M.; Maeda, Y. *J. Am. Chem. Soc.* **1999**, *121*, 10068−10080.

(12) Okamoto, H.; Kishida, H.; Matsuzaki, H.; Manabe, T.; Yamashita, M.; Taguchi, Y.; Tokura, Y. *Nature* **2000**, *405*, 929−932.

(13) Clérac, R.; Miyasaka, H.; Yamashita, M.; Coulon, C. *J. Am. Chem. Soc.* **2002**, *124*, 12837−12844.

(14) Takamizawa, S.; Nataka, E.; Akatsuka, T.; Miyake, R.; Kakizaki, Y.; Takeuchi, H.; Maruta, G.; Takeda, S. *J. Am. Chem. Soc.* **2010**, *132*, 3783−3792.

(15) Takamizawa, S.; Nakata, E.; Miyake, R. *Dalton Trans.* **2009**, 1752−1760.

(16) Takamizawa, S.; Nakata, E.; Akatsuka, T.; Kachi-Terajima, C.; Miyake, R. *J. Am. Chem. Soc.* **2008**, *130*, 17882−17892.

(17) Takamizawa, S.; Saito, T.; Akatsuka, T.; Nakata, E. *Inorg. Chem.* **2005**, *44*, 1421−1424.

(18) Takamizawa, S.; Nakata, E.; Akatsuka, T. *Angew. Chem., Int. Ed.* **2006**, *45*, 2216−2221.

(19) Kitagawa, S.; Kitaura, R.; Noro, S. *Angew. Chem., Int. Ed.* **2004**, *43*, 2334−2375.

(20) Lin, Z.-J.; Lu, J.; Hong, M.; Cao, R. *Chem. Soc. Rev.* **2014**, *43*, 5867−5895.

(21) Sarkisov, L.; Martin, R. L.; Haranczyk, M.; Smit, B. *J. Am. Chem. Soc.* **2014**, *136*, 2228−2231.

(22) Kosaka, W.; Yamagishi, K.; Yoshida, H.; Matsuda, R.; Kitagawa, S.; Takata, M.; Miyasaka, H. *Chem. Commun.* **2013**, *49*, 1594−1596.

(23) Takahashi, K.; Hoshino, N.; Takeda, T.; Noro, S.; Nakamura, T.; Takeda, S.; Akutagawa, T. *Dalton Trans* **2014**, *43*, 9081−9089.

(24) Burrows, A. D.; Mahon, M. F.; Raithby, P. R.; Warren, A. J.; Teat, S. J.; Warren, J. E. *CrystEngComm* **2012**, *14*, 3658−3666.

(25) *Crystal structure: single-crystal structure analysis software*, version 4.0.1; Rigaku Corp. and Molecular Structure Corp.: Salem, NH, and The Woodlands, TX , 2010.

(26) Sheldrick, G. M. *SHELX97 Programs for Crystal Structure Analysis*; Universitat Göttingen: Göttingen, Germany, 1998.

(27) *SIR2008*: Burla, M. C.; Caliandro, R.; Camalli, M.; Carrozzini, B.; Cascarano, G. L.; De Caro, L.; Giacovazzo, C.; Polidori, G.; Siliqi, D.; Spagna, R. *J. Appl. Crystallogr.* **2007**, *40*, 609−613.

(28) Spek, A. L. *J. Appl. Crystallogr.* **2003**, *36*, 7−13.

(29) Wolff, S. K.; Grimwood, D. J.; McKinnon, J. J.; Turner, M. J.; Jayatilaka, D.; Spackman, M. A. *CrystalExplorer*, version 3.1; University of Western Australia: Crawley, Western Australia, Australia, 2012.

(30) Spackman, M. A.; Jayatilaka, D. *CrystEngComm* **2009**, *11*, 19−32.

(31) Takamizawa, S.; Nakata, E.; Yokoyama, H.; Mochizuki, K.; Mori, W. *Angew. Chem., Int. Ed.* **2003**, *42*, 4331−4334.

(32) Horike, S.; Shimomura, S.; Kitagawa, S. *Nat. Chem.* **2009**, *1*, 695−704.

(33) Kachi-Terajima, C.; Akatsuka, T.; Kohbara, M.; Takamizawa, S. *Chem. - Asian J.* **2007**, *2*, 40−50.

(34) Nangia, A. *J. Chem. Sci.* **2010**, *122*, 295−310.

(35) Nagels, N.; Hauchecorne, D.; Herrebout, W. A. *Molecules* **2013**, *18*, 6829−6851.

(36) Schollmeyer, D.; Shishkin, O. V.; Ruhl, T.; Vysotsky, M. O. *CrystEngComm* **2008**, *10*, 715−723.

(37) Shishkin, O. V. *Chem. Phys. Lett.* **2008**, *458*, 96−100.

(38) Politzer, P.; Lane, P.; Concha, M. C.; Ma, Y.; Murray, J. S. *J. Mol. Model.* **2007**, *13*, 305−311.

(39) Matta, C. F.; Hernández-Trujillo, J.; Tang, T.-H.; Bader, R. F. W. *Chem. - Eur. J.* **2003**, *9*, 1940−1951.

(40) Choi, H. S.; Suh, M. P. *Angew. Chem., Int. Ed.* **2009**, *48*, 6865−6869.

(41) Sung, S.; Suh, M. P. *J. Mater. Chem. A* **2014**, *2*, 13245−13249.

DOI: 10.1021/acs.inorgchem.5b01168
Inorg. Chem. 2015, 54, 9423−9431